Large-Area and Highly Crystalline WSe_2 Monolayers: from Synthesis to Device Applications

Highly crystalline and large-area WSe_2 monolayers are obtained by the selenization of WO_3 in the presence of hydrogen. The high mobility values in field-effect transistors and high gains in resistor-loaded inverters demonstrate that synthetic WSe_2 layers are potentially useful for logic circuits.

By Jing-Kai Huang,[12†] Jiang Pu,[3†] Chih-Piao Chuu,[1] Chang-Lung Hsu,[1] Ming-Hui Chiu[1], Zhen-Yu Juang,[1] Yong-Huang Chang,[1] Wen-Hao Chang,[4] Yoshihiro Iwasa,[5] Mei-Ying Chou,[1,6,7] Taishi Takenobu[3] and Lain-Jong Li[1]**

[1]*Institute of Atomic and Molecular Sciences, Academia Sinica, Taipei, 10617, Taiwan*

[2] *Department of Photonics, National Chiao-Tung University, HsinChu, 300, Taiwan*

[3] *Department of Applied Physics, Waseda University, Tokyo 169-8555, Japan*

[4] *Department of Electrophysics, National Chiao-Tung University, HsinChu, 300, Taiwan*

[5]*Department of Applied Physics, The University of Tokyo, Tokyo 113-8656, Japan*

[6]*Department of Physics, National Taiwan University, Taipei, Taiwan*

[7]*School of Physics, Georgia Institute of Technology, Atlanta, GA 30332, USA*

[†]These authors contributed equally.
To whom correspondence should be addressed: (T.Takenobu) takenobu@waseda.jp; (L. J. Li) lanceli@gate.sinica.edu.tw

The monolayer transition metal dichalcogenides have recently attracted much attention owing to their potential in valleytronics, flexible and low-power electronics and optoelectronic devices. Recent reports have demonstrated the growth of large-size 2-dimensional MoS_2 layers by the sulfurization of molybdenum oxides. However, the growth of transition metal selenide monolayer has still been a challenge. Here we report that the introduction of hydrogen in the reaction chamber helps to activate the selenization of WO_3, where large-size WSe_2

monolayer flakes or thin films can be successfully grown. The top-gated field-effect transistors based on WSe_2 monolayers using ionic gels as the dielectrics exhibit ambipolar characteristics, where the hole and electron mobility values are up to 90 and 7 cm^2/Vs respectively. The resistor-loaded inverter based on a WSe_2 film, with a gain ~13, further demonstrates its applicability for logic-circuit integrations.

Keywords: Transition metal dichalcogenides; Tungsten diselenides; Layered materials; Transistors; Inverters; Two-dimensional materials.

Transition metal dichalcogenides (TMD) have attracted much attention due to their two-dimensional (2-d) layer structure, where a sheet of metal atoms is sandwiched between two sheets of chalcogens by covalent interaction. Depending on the selection of the metal, these layered materials may exhibit superconducting, metallic or semiconducting properties.[1-4] Moreover, the electronic structures of the semiconducting TMD such as molybdenum disulfide (MoS_2), Tungsten disulfide (WS_2) and Tungsten diselenide (WSe_2) vary with their thickness. For example, the optical transition of MoS_2 transforms from the indirect gap in a bulk form to the direct gap when it is a monolayer sheet.[5-13] These monolayer TMD films are highly bendable and thus promising for flexible electronics.[14] Another important feature of the 2-d TMD films is their ultra small thickness that allows efficient Fermi energy tuning by electrostatic interaction or a gate voltage.[15,16] Recently, it has been demonstrated that the field-effect transistors fabricated with the MoS_2 thin layers exhibit an excellent on/off current ratio and a high carrier mobility,[17] which stimulates the research efforts to use them for next generation transistors.[17,18] So far, most of the MoS_2 based transistors show an n-type behavior and the efficient *p*-doping method for MoS_2 is still not yet available. Hence, the research for *p*-type or high hole mobility TMD monolayer or becomes urgent for realizing complementary digital logic applications. Actually, the *p*-type transistor behaviors have been observed in bulk and mechanically exfoliated monolayer or few-layer tungsten diselenide flakes.[19,20] Recent studies have made significant advances in understanding the role of contact metals on the electrical characteristics of the transistors made from exfoliated WSe_2 flakes.[19,21] However, the large scale device applications still rely on the breakthrough in growths of large-size WSe_2 thin layers. Early approaches including the thermal decomposition of WSe_3,[22] direct heating of the mixture of W and Se elements,[23-27] the vapor transport growth of WSe_2,[28] and the reaction of WO_3 fine powders with H_2Se[29] or Se[30] have led to successful growth of WSe_2 crystals or fullerene-like particles but not atomically thin layers. Recent progresses on the growth of monolayer MoS_2 by the sulfurization of molybdenum oxides[31-34] in vapor phases, where the formation of MoS_2 atomically thin layers are based on the reaction of MoO_3 and sulfur vapors, have shed the light on the large-area preparation of other TMD monolayer materials. In this contribution, we report that the introduction of hydrogen in the reaction environment is necessary for the growth of highly crystalline WSe_2 monolayer using the vapor phase reaction of WO_3 and Se. The field-effect transistors based on the as-grown WSe_2 monolayers exhibit ambipolar behaviors with high mobility values in both *p*- and *n*-channels. The resistor-loaded inverter based on a WSe_2 film shows a gain ~13, demonstrating that the synthetic WSe_2 film is readily applicable for logic-circuit integrations.

Results

Growth of WSe_2 monolayers. Figure 1a schematically illustrates our experimental set-up for growing thin WSe_2 layers by the selenization of WO_3 powders in a hot-wall chemical vapor deposition (CVD) chamber. The morphology of the WSe_2 grown on the sapphire substrates varies with the substrate temperatures. The optical micrograph (OM) in Figure 1b shows that the WSe_2 grown at 850°C exhibits a triangular shape and the lateral size of each triangle is larger than 10 μm and up to 50 μm, where the lateral size may have a limit due to the high energy caused by the lattice mismatch between the WSe_2 and sapphire substrates. Meanwhile, the sparsely distributed triangles indicate that the nucleation density of the WSe_2 is low. Figure 1c is the OM image for the WSe_2 grown at a lower temperature says at 750°C, where many small WSe_2 domains merge to form a continuous film. The domain size of the WSe_2 formed at 750°C is around several to 5 μm, as shown in the SEM image in Figure S1 for the nearly completely merged WSe_2 grown at 750°C. These observations are rationale since a lower growth temperature typically results in a higher nucleation density. It is noteworthy that the orientation of these small WSe_2 triangles grown at 750°C aligns to a certain direction, implying the expitaxial growth feature of the process. Figure 1d shows the atomic force microscopic (AFM) image for the WSe_2 triangle grown at 850°C, where the thickness 0.73 nm of the film is in agreement with the reported thickness for mechanically exfoliated WSe_2 monolayers.[19,21] The AFM image and cross-section profile in Figure S2 obtained for the WSe_2 film grown at 750°C also prove that the continuous film is a monolayer. For the WSe_2 flakes grown at 850°C, most of the flakes are characterized as monolayers but we still occasionally observe the growth of 2nd layer WSe_2 on top of some large monolayer flakes as shown in the OM in Figure 2a. The AFM cross-sectional height profile for the sample shown in Figure S3 confirms that the additional layer on top is a monolayer.

Raman Spectroscopy. Raman spectra for the monolayer and bilayer WSe_2 excited by a 473 nm laser are shown in Figure 2b, where the two characteristic peaks for monolayer WSe_2 at 248 cm^{-1}, assigned to E^1_{2g} mode, and 259 cm^{-1}, assigned to A_{1g} mode, are observed.[35,36] For the bilayer WSe_2, the A_{1g} mode slightly left shifts compared with that of monolayer WSe_2, which is consistent with the observation in ref.35. Other high energy bands at 358.5 and 373.5 cm^{-1}, attributed to the $2E_{1g}$ and A_{1g}+LA modes, are also identified.[37-39] Most importantly, the Raman band at 308 cm^{-1} which has been reported to be related to the interlayer interaction[40] is not observed in our WSe_2 monolayer. Instead, this characteristic peak exhibits in the Raman spectrum for our bilayer WSe_2, consistent with the results in ref.35.

Optical absorption and photoluminescence. Figure 2c displays the optical absorption spectrum for the monolayer WSe_2 film. The excitonic absorption peaks A and B, arising from direct gap transitions at the K point, are identified at around 750 and 595 nm respectively, agreeing well previous reports.[41-43] Figure 2d compares the PL spectra (excited by a 532 nm laser) of monolayer and bilayer WSe_2 areas. The PL spectrum for the monolayer WSe_2 flake exhibits a strong emission at ~760 nm corresponding to the A excitonic absorption, whereas the emission intensity of the same peak is much lower in the bilayer WSe_2. Moreover, in addition to the A exciton peak, another peak at a longer wavelength (~806 nm) attributing to the indirect band gap emission, is observed for the bilayer WSe_2. It is noted that the indirect gap emission is absent in a monolayer and the distinctly strong emission from a monolayer is in good

agreement with the recent report.[44-46] All these PL observations further confirm the layer number assignment for our CVD WSe_2 samples.

Structural Characterization. The X-ray photoemission spectroscopy (XPS) was used to measure the binding energies of the W and Se in our CVD WSe_2 monolayer film, confirming their stoichiometry. Figures 3a and 3b show the binding energy profiles for W 4f and Se 1s. The peaks at 32.8 eV and 35.0 eV are attributed to the doublet W $4f_{7/2}$ and W $4f_{5/2}$ binding energies respectively. The peaks at 55 eV and 55.9 eV are corresponding to the Se $3d_{5/2}$ and Se 3d binding energies. All these results are consistent with the reported values for WSe_2 crystal.[47,48] It is noted that figure 3a does show the presence of weak peaks for WO_3 at 35.8 eV and 38.0 eV (the doublet W $4f_{7/2}$ and W $4f_{5/2}$ for WO_3 respectively). This is caused by the occasionally deposited WO_3 particles on the surface of WSe_2. The domain edge of the WSe_2 may also contribute to the WO_3 signals. Figure S4 displays the SEM image showing the formation of some WO_3 particles during the growth of WSe_2 film. Nevertheless, the ratio between W and Se elements obtained from the integrated peak area after excluding the WO_3 part is 1:1.988, suggesting that our CVD WSe_2 exhibits reasonable good stoichiometry.

The tunneling electron microscopy (TEM) image in Figure 3c shows the periodic atom arrangement of the WSe_2 monolayer, demonstrating that the CVD WSe_2 film is highly crystalline. The inset shows the selected area electron diffraction (SEAD) pattern taken with an aperture size (~160 nm) for the sample. Figure 3d is the magnified TEM image for the area squared by dashed lines in Figure 3c, where the high resolution TEM image and the corresponding SAED pattern with [001] zone axis (inset of figure 3c) reveal the hexagonal lattice structure with the lattice spacing of 0.38 and 0.33 nm assigned to the (100) and (110) planes.[49]

Discussion

It is noteworthy pointing out that for the synthesis of MoS_2 monolayer using the same method,[31] the sulfurization of MoO_3 is typically performed at 650°C in an Ar environment, where the chemical reaction is described as:

$$2MoO_3 + 7S \rightarrow 2MoS_2 + 3SO_2 \qquad \text{(Eq.1)}$$

The introduction of a reducer such as hydrogen in the reaction atmosphere is not necessary. However, the chemical reactivity of Se is much lower than S and thus a strong reducer like hydrogen is required in the selenization reaction of WO_3. In our experiments, we also observe that no WSe_2 is obtained if no hydrogen gas is introduced in the chamber. The thermodynamic calculations have also corroborated that the selenization reaction of WO_3 is only possible with the presence of hydrogen.[30] The chemical reaction occurs during the selenization of WO_3 is as follows:

$$WO_3 + 3Se + H_2 \rightarrow WSe_2 + H_2O + SeO_2 \qquad \text{(Eq.2)}$$

To demonstrate the quality of the synthetic WSe_2 monolayer, we measured the electrical properties of the electric double layer transistors (EDLT) based on the as-grown WSe_2 monolayer film on sapphire substrates. Figure 4a shows the OM image for the EDLT device top view, where the channel width and length are 668 μm and 1225 μm respectively. Figure 4b shows the output characteristics for both the *p*- and *n*-channels at various reference voltages (V_R) as specified in graphs. Note that the V_R is the measured voltage between the electrolytes and WSe_2, i.e. the voltage for electric double layer on WSe_2 surfaces, and it is normally smaller than the applied gate voltage (on the

top Pt metal) since the gate voltage is partially consumed by the electric double layer on the gate electrode. It is observed that the source-drain current exhibits an obvious saturation regime for all curves. To obtain the capacitance of the WSe_2/ion gel surface, the source and drain electrodes are short-circuited, and two terminal measurements across the source/drain and top-gate electrodes are carried out. We perform the impedance measurements using a frequency response analyzer (a Solartron 1252A frequency response analyzer with a Solartron 1296 dielectric interface controlled by ZPlot and ZView software), and the frequency range is set to 10^{-3}-10^5 Hz. Especially, for DC voltage dependence of ion-gel capacitance, the frequency is set to 10 Hz with an AC voltage amplitude of 5 mV, and DC voltage is applied from -3.2 to 3.4 V. The measurement result for the specific capacitance at various reference voltages is shown in Figure 4c. The dependence of the capacitance on V_R reveals a step function-like profile for both *p*-and *n*-channels, which is reasonably explained by competition of geometrical and quantum capacitances. Owing to the high ionic concentration of the ion gel and the large-specific surface area of the 2-d TMD film,, the measured capacitance is consisted of two major contributions: the interfacial capacitance arising from the electric double layer (EDL) formed by ions at the WSe_2 – ion gel interface and the quantum capacitance, where these two are modeled as two capacitors in series.[50] The measured capacitance is dominated by the quantum capacitance when the V_R is inside the E_g of WSe_2 whereas the capacitance is governed by the geometrical capacitance when the V_R is outside the E_g. Note that the effect of in-gap states is negligible due to the huge geometrical capacitance of the ion gel. Based on this argument, the E_g of WSe_2 can be estimated to be the difference between the rising onset points in *p*-channel (-0.82 V) and *n*-channel (0.79 V), i.e. ~1.61 V, where the number approximately agrees with the energy band-gap (E_g ~ 1.6 eV) of WSe_2 monolayer. Moreover, the field-effect mobility was calculated by the standard formula for the linear region, $\mu = (L/WC_iV_D)\cdot(\Delta I_D/\Delta V_R)$, where μ is the field-effect mobility, W is the channel width, V_D is the drain voltage, C_i is the measured specific capacitance of the ion gel, L is the channel length and I_D is the drain current.

Figure 4d displays the *p*- and *n*-transfer curves (drain current vs. V_R) of a WSe_2 monolayer EDLT at the applied drain voltage V_D = - 0.1 V and 0.1 V respectively. Consistent with the report for thick WSe_2 crystals by Podzorov et al.,[20] we clearly observe an ambipolar transport behaviour with Ohmic-like current-voltage characteristics. The inset in each graph replots the drain current from a linear to a log scale, and the on-off current ratio is as high as 10^5 and 10^4 for *p*- and *n*-channels. The reference voltage dependence of carrier mobilities from capacitance measurements as shown in Figure 4c also shows a step-like profile. The highest carrier mobility is 90 cm^2/Vs for the hole transport and 7 cm^2/Vs for the electron transport. It is noted that Figure S5 provides the transfer curves, mobility and capacitance dependences on V_R performed in the saturation regime, and these results are consistent those measured in the linear regime. Figure 4c explores that the Ni source and drain metals form a mid-gap Schottky barrier with WSe_2 film. Meanwhile, Figure 4d shows that the threshold voltage for the *p*-channel is 0.97 V in the forward scan, close to the 0.82 V for the *n*-channel. The contact resistance difference for both channels may not be able to fully explain the mobility difference for holes and electrons. We have evaluated the effect masses of electrons and holes from the band structure obtained by first-principle calculations. Figure 5a shows the electronic band structure for monolayer WSe_2 calculated at the experimental lattice constant of 2H-WSe_2 (3.286 Å).[51] The spin-orbit

coupling (SOC) is significant in WSe_2, creating a splitting of 470 meV at the valence band maximum. The LDA direct band gap at the K point is reduced from 1.58 eV (without SOC) to 1.29eV (with SOC). Figure 5b shows the calculated effective masses of electrons and holes at K as a function of strain ranging from -0.5 % to 1.5 %, for which the band gap remains to be direct. With the SOC included, the effective masses are m^*_e=0.39(0.28) m_e and m^*_h=0.37(0.55) m_e for electrons and holes, respectively at the experimental lattice constant; the values in parentheses correspond to the second lowest conduction band and the second highest valence band that are split by the SOC effect. As the layer is stretched, the effective masses of both electrons and holes are lowered by a few percents. It turns out that the effective mass of holes is always smaller than that of electrons by 5-10% in the range of strain considered. This variation is not sufficient to explain the huge difference in the mobility of electrons and holes observed in our experiment. Therefore, the measured high mobility ratio between holes and electrons may be related to their significantly different cross sections for scattering with charged impurities introduced by the substrate or the transfer process. This will be a topic of further investigation in the future.

To examine the logic-operation capability, we have fabricated a simple resistor-loaded inverter by connecting WSe_2 monolayer EDLTs in series with 500 kΩ commercial resistors. The circuit diagram and input (V_{in})–output (V_{out}) voltage characteristics are presented in Figure 6a. Using the *p*-type operation of a WSe_2 monolayer EDLT with the mobility of 50 cm^2/Vs and the on-off current ratio of 10^6, ideal inverter actions were observed. The output voltage switched near V_{in} = 1 V and the inverter was completely switched within 0.5 V of the V_{in} variation. The voltage gain, defined as the negative of dV_{out}/dV_{in}, plotted in Figure 6b was approximately 13. For the successful implementation of digital logics in electronic circuits based on any new nanomaterial, a voltage gain more than 1 is needed so that the output of one inverter could drive the input of the next inverter in the cascade. Therefore, our inverter is readily applicable for the integration in arrays of logic gates. Moreover, it is noted that the obtained gain of 13 is higher than the recently reported single-layer MoS_2 inverters (gain ~ 5)[52] due to the high carrier mobility of WSe_2 monolayers and the large specific capacitance of ion-gels.

Method

Growth of WSe_2 layers. The WO_3 powders (0.3 g) were placed in a ceramic boat located in the heating zone center of the furnace. The Se powders were placed in a separate ceramic boat at the upper stream side maintained at 270°C during the reaction. The sapphire substrates for growing WSe_2 were put at the downstream side, where the Se and WO_3 vapors were brought to the targeting sapphire substrates by an Ar/H_2 flowing gas (Ar = 80 sccm, H_2 = 20 sccm, chamber pressure = 1 Torr). The center heating zone was heated to 925°C at a ramping rate 25°C/min. Note that the temperature of the sapphire substrates was at ~ 750 to 850°C when the center heating zone reaches 925°C. After reaching 925°C, the heating zone was kept for 15 minutes and the furnace was then naturally cooled down to room temperature.

Fabrication of EDLT devices. For the source and drain electrodes, Au contacts with Ni adhesion layers (70 nm / 2 nm) were thermally deposited onto the surface of the WSe_2 films. The ion gels, a mixture of a triblock copolymer, poly(styrene-block-methyl methacrylate-block-styrene) (PS-PMMA-PS; M_{PS} = 4.3 kg/mol, M_{PMMA} = 12.5 kg/mol, Mw = 21.1 kg/mol), and an ionic liquid, 1-ethyl-3-methylimidazolium

bis(trifluoromethylsulfonyl)imide ([EMIM][TFSI]) in an ethyl propionate solution, are used as the top gate dielectrics.[14] Note that the weight ratio of the polymer, ionic liquid, and solvent was maintained at 0.7:9.3:20. This solution was drop-casted onto and cover the surfaces of WSe_2 film and the source and drain electrodes. The transistor channel was then covered with a thin Pt foil (thickness of 0.03 mm) to form the top-gate electrode. Finally, a thin gold wire was inserted into the gel films, in between the channel and top gate metal, as the reference electrode. All electrical characterizations were performed using a semiconductor parameter analyzer (Agilent E5270) in a shield probe station inside an N_2-filled glove box.

Characterizations. The AFM images were performed in a Veeco Dimension-Icon system. Raman spectra were collected in a confocal Raman system (NT-MDT). The wavelength of laser is 473 nm (2.63eV), and the spot size of the laser beam is ~0.5μm and the spectral resolution is 3 cm^{-1} (obtained with a 600 grooves/mm grating). The Si peak at 520 cm^{-1} was used as a reference for wave number calibration. The WSe_2 films were transferred onto a copper grid for TEM observation. HRTEM imaging was performed on JEOL-2100F FEG-TEM operated at 100 kV. Chemical configurations are determined by X-ray photoelectron spectroscope (XPS, Phi V6000). XPS measurements were performed with an Mg Kα X-ray source on the samples. The energy calibrations were made against the C 1s peak to eliminate the charging of the sample during analysis.

Numerical Simulation. The band structure is derived by first-principles calculations based on density functional theory (DFT) [53] using the Vienna Ab initio simulation package (VASP) [54,55]. The electron-ion interaction and exchange-correlation potential are described by the projector augmented wave (PAW) [56] method and the local density approximation (LDA) [57]. A slab model is used to simulate the system with a vacuum thickness greater than 15 Å, and a 440-eV energy cut-off of plane waves and a k-mesh of 12×12×1 points are used to satisfy the energy and force convergent criteria.

CONCLUSIONS

In conclusion, we have synthesized highly crystalline and large-area WSe_2 monolayers by the gas phase selenization of WO_3 in a hot-wall CVD chamber. It is concluded that the hydrogen gas plays an important role to activate the reaction. Triangle and single crystalline WSe_2 monolayer flakes can be grown at 850^{o}C, whereas a lower temperature 750^{o}C results in a continuous and polycrystalline monolayer film. The WSe_2 transistors based on ion gel gating exhibit an ambipolar behavior with high carrier mobility values. Moreover, the WSe_2 based inverter exhibits a high gain ~13, demonstrating that synthetic WSe_2 layers can serve as a building block for future logic circuits based on 2-d materials.

Acknowledgements: This research was mainly supported by Academia Sinica (IAMS and Nano program) and National Science Council Taiwan (NSC-99-2112-M-001-021-MY3 and 99-2738-M-001-001). T.T. was partially supported by the Funding Program for the Next Generation of World-Leading Researchers. Y.I. was supported by a Grant-in-Aid for Scientific Research (S) (21224009), by the FIRST Program from JSPS, and by SICORP from JST.

Author Contributions

J.K.H. and Y.H.C performed the major part of the growth experiments. P.J. performed the EDLT fabrication and measurements. C.L.H. performed the XPS measurement. Z.Y.J. performed the TEM study. W.H.C. and M.H.C. helped on the absorption and PL measurements. C.P.C and M.Y.C. performed the numerical simulations. All authors discussed the results. L.J.L. and J.K.H. conceived the study and wrote the manuscript. T.T. wrote the EDLT part of the manuscript. M.Y.C. wrote the numerical simulation part.

Additional information
Supplementary Information accompanies this paper on http://www.nature.com/naturecommunications

Competing financial interests: The authors declare no competing financial interests.

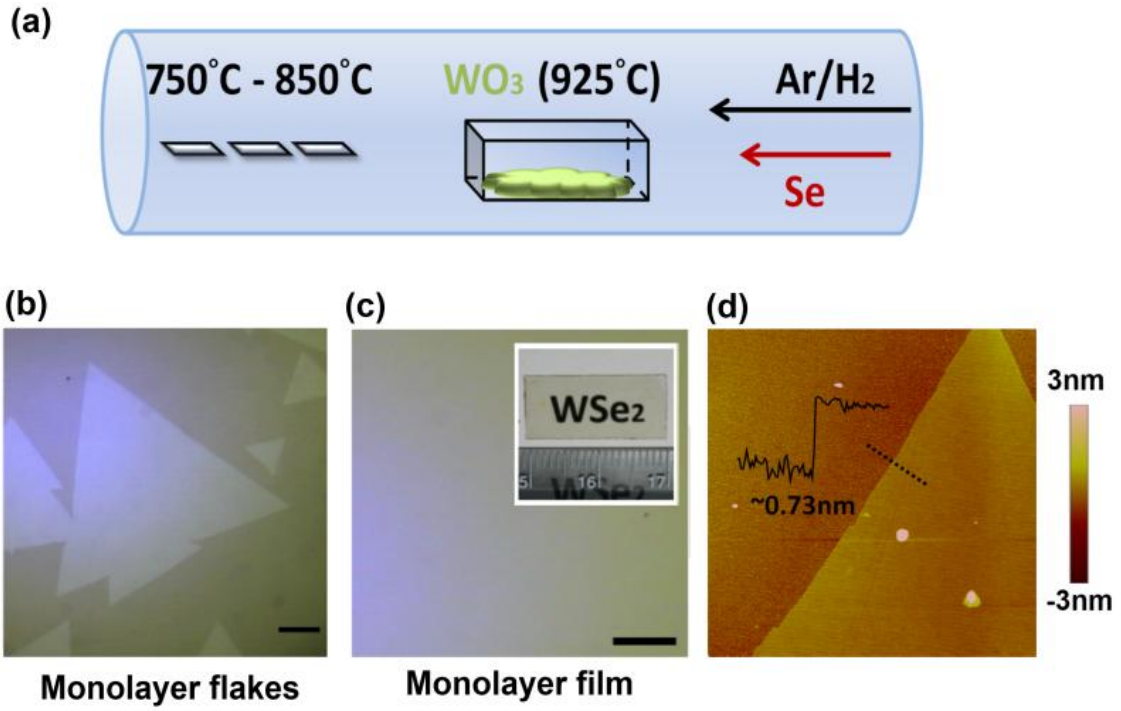

Figure 1. Synthesis of WSe_2 monolayers. (a) Schematic illustration for the growth of WSe_2 layers on sapphire substrates by selenization of WO_3 powders in a CVD furnace. (b,c) The optical microscopy images of the WSe_2 monolayer flakes and monolayer film grown at 850 and 750 ^oC respectively. Scale bar is 10 μm in length. The inset in (c) shows the photograph of a uniform monolayer film grown on a double side polished sapphire substrate. (d) AFM image of a WSe_2 monolayer flake grown at 850^oC on a sapphire substrate.

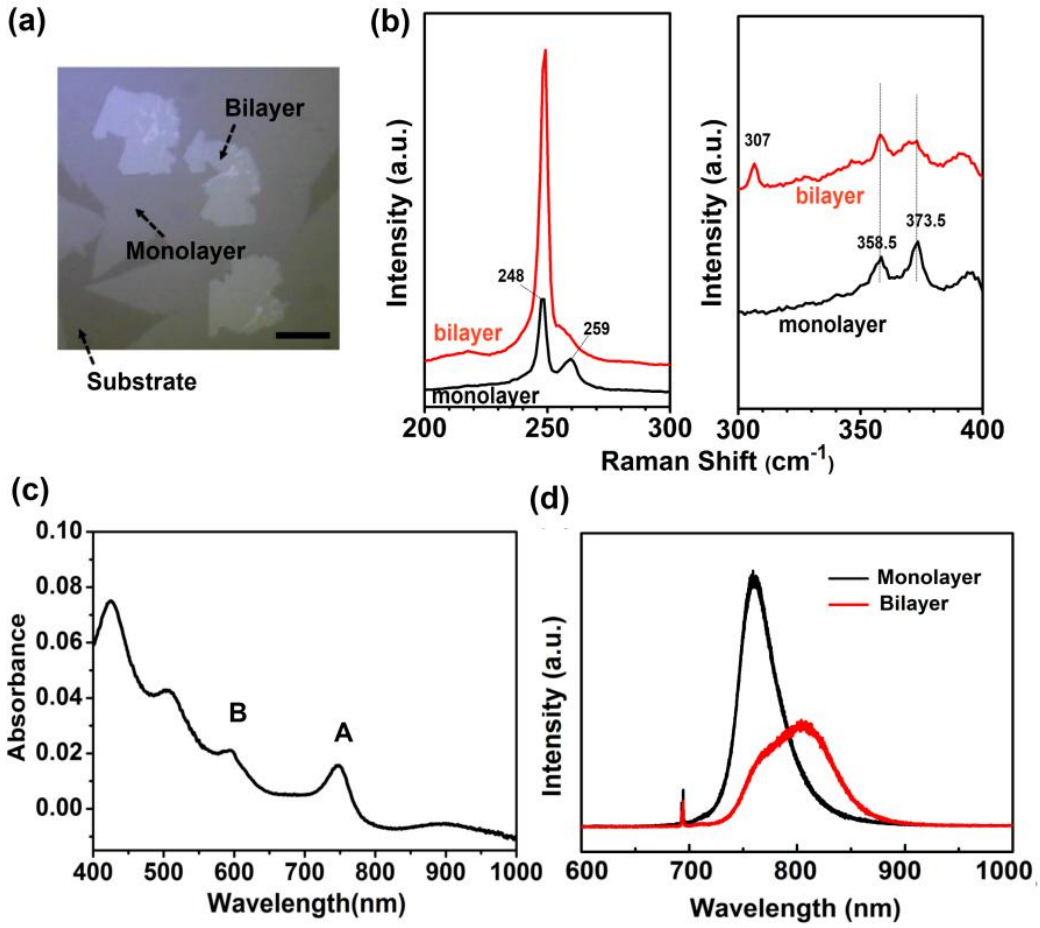

Figure 2. Optical spectroscopy. (a) The optical microscopic image of the 2nd layer WSe_2 on top of some large monolayer flakes. Scale bar is 10 μm in length. (b) Raman spectra for the monolayer and bilayer WSe_2, obtained in a confocal Raman spectrometer excited by a 473 nm laser. (c) Optical absorption spectrum for the continuous WSe_2 film. (d) Photoluminescence spectra for the CVD WSe_2 monolayer and bilayer, obtained in a microscopic PL system (excitation wavelength 532 nm).

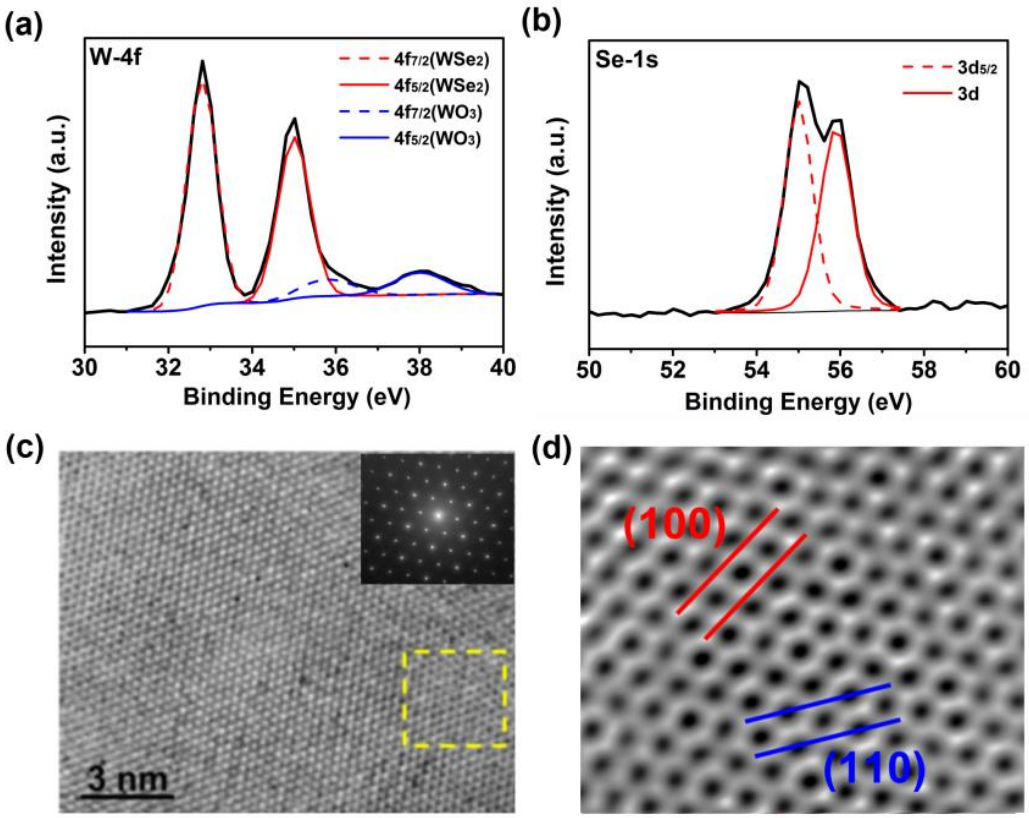

Figure 3. XPS and structural characterizations. (a,b) XPS spectra of the WSe_2 monolayer film, where the (a)W 4f and (b) Se 1s binding energies are identified. The two peaks at 32.8 eV and 35.0 eV, attributed to the doublet W $4f_{7/2}$ and W $4f_{5/2}$. Note that the peaks at 35.8 eV and 38.0 eV are attributed to the doublet W $4f_{7/2}$ and W $4f_{5/2}$ for WO_3.The binding energy at 55 eV and 55.9 eV can be assigned to the Se $3d_{5/2}$ and Se 3d binding energies, respectively. (c) High resolution TEM image of WSe_2 monolayer with an inset showing its SAED pattern. (d) Enlarged TEM image for the marked area in figure (c)

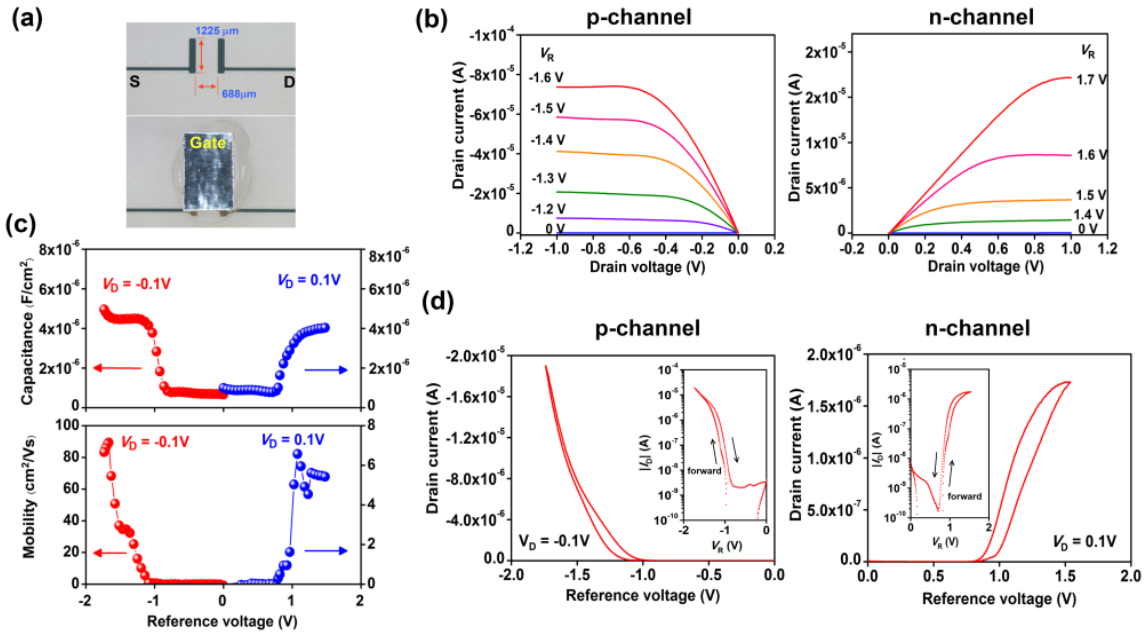

Figure 4. Electric double layer transistor. (a) Optical micrograph of the top view for the WSe_2 EDLT device, where the top and bottom photos were taken before and after the ion gel/top gate deposition. (b) Output characteristics of the WSe_2 EDLT device. (c) Specific capacitance and carrier mobility values measured at various reference voltages. The drain current level was maintained at $\pm$0.1V, which was in the linear regime. (d) The typical transfer curves for the EDLT device, where inset in each graph shows the transfer curve plotted in a log scale.

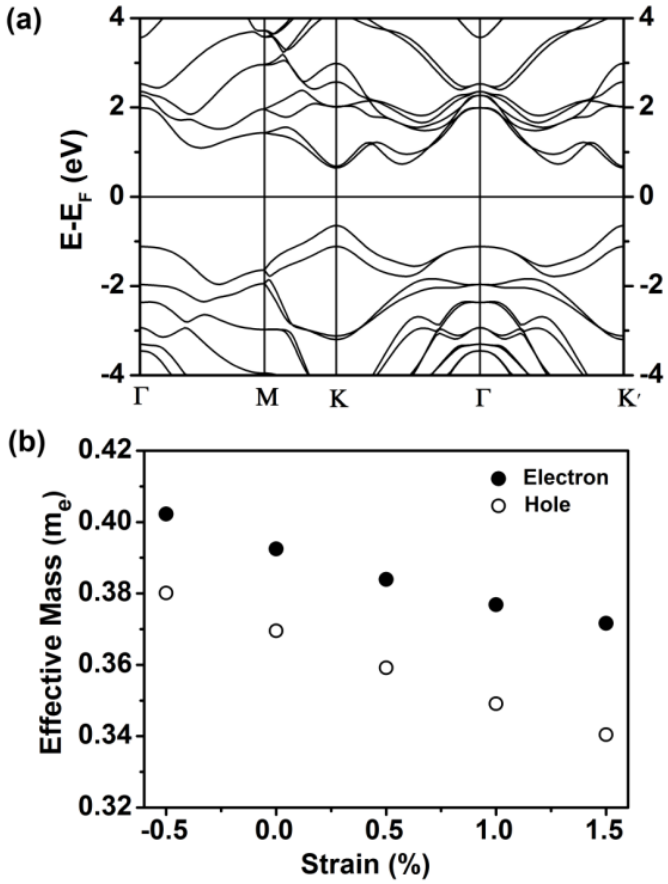

Figure 5. Calculated band structure and charge carriers effective masses at K point of WSe_2 monolayer. (a) Electronic band structure for monolayer WSe_2 calculated at the experimental lattice constant of 2H-WSe_2 (3.286 Å). The spin-orbit coupling is included. (b) Calculated effective masses of electrons and holes at K as a function of strain.

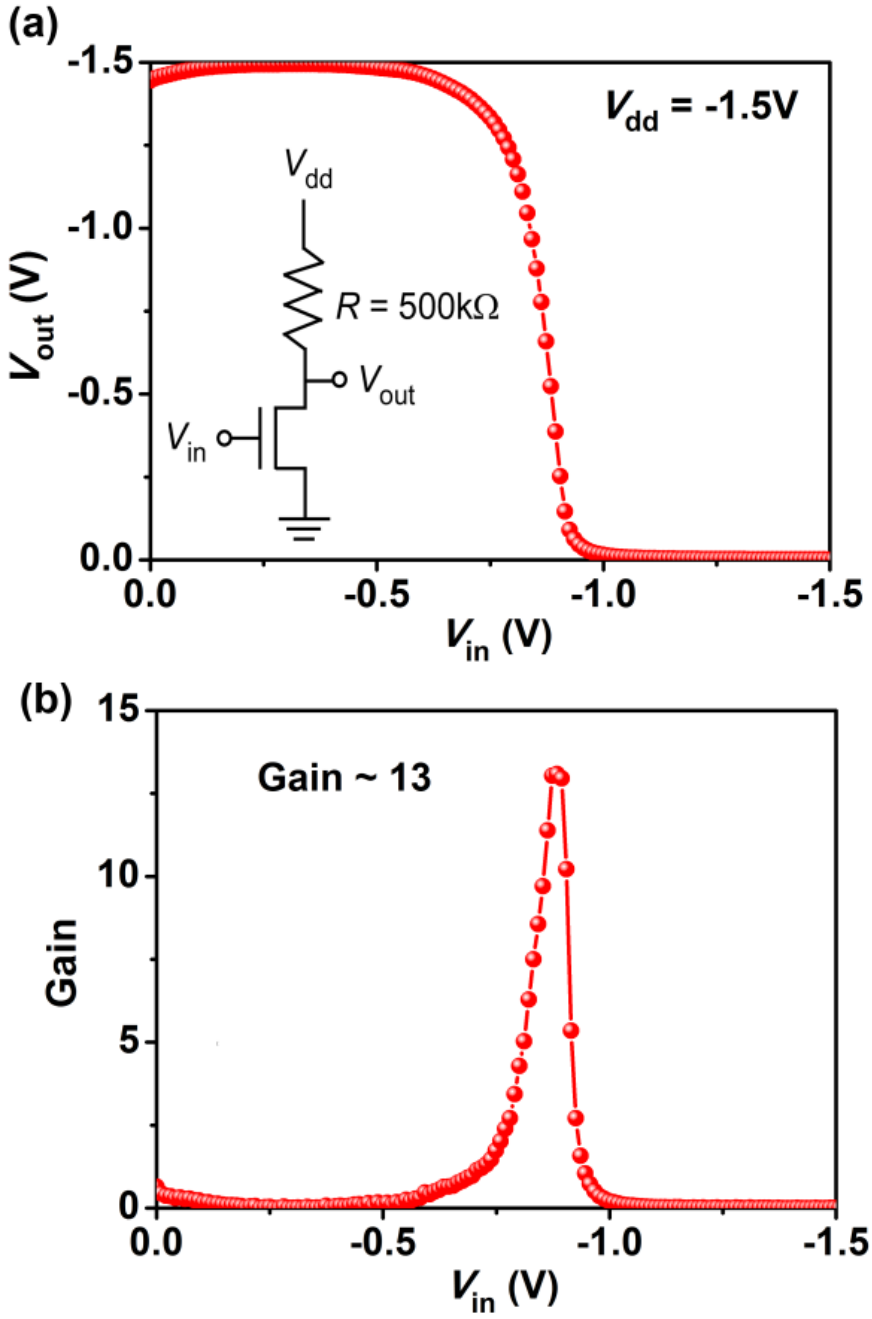

Figure 6. Resistor-loaded inverters. (a) The circuit diagram and input (V_{in})–output (V_{out}) voltage characteristics, and (b) the voltage gain (defined as the negative of dV_{out}/dV_{in}) of the resistor-loaded WSe2 inverter.

REFERENCES:

(1) Chhowalla, M., Shin, H. S., Eda, G., Li, L.-J., Loh, K. P. & Zhang, H. The chemistry of two-dimensional layered transition metal dichalcogenide nanosheets. *Nat. Chem.* **5,** 263–275 (2013).
(2) Ataca, C., Şahin, H. & Ciraci, S. Stable, single-layer MX_2 transition-metal oxides and dichalcogenides in a honeycomb-like structure. *J. Phys. Chem. C* **116,** 8983−8999 (2012).
(3) Huang, X., Zeng, Z. & Zhang, H. Metal dichalcogenide nanosheets: preparation, properties and applications. *Chem. Soc. Rev.* **42,** 1934 (2013).
(4) Kashid, R. V., Late, D. J., Chou, S. S., Huang, Y.-K., De, M., Joag, D. S., More, M. A. & Dravid, V. P. Enhanced field-emission behavior of layered MoS_2 sheets. *Small* doi: 10.1002/smll.201300002 (2013).
(5) Splendiani, A., Sun, L., Zhang, Y., Li, T., Kim, J., Chim, C.-Y., Galli, G. & Wang, F. Emerging photoluminescence in monolayer MoS_2. *Nano Lett.* **10,** 1271-1275 (2010).
(6) Aharon, E., Albo, A., Kalina, M. & Frey, G. L. Stable blue emission from a polyfluorene/layered-compound guest/host nanocomposite. *Adv. Funct. Mater.* **16,** 980-986 (2006).
(7) Mak, K. F., Lee, C., Hone, J., Shan, J. & Heinz, T. F. Atomically thin MoS_2: A new direct-gap semiconductor. *Phys. Rev. Lett.* **105,** 136805-1-4 (2010).
(8) Lee, C., Yan, H., Brus, L. E., Heinz, T. F., Hone, J. & Ryu, S. Anomalous lattice vibrations of single- and few-layer MoS_2. *ACS Nano* **4,** 2695-2700 (2010).
(9) Molina-Sánchez, A. & Wirtz, L. Phonons in single-layer and few-layer MoS_2 and WS_2. *Phys. Rev. B* **84,** 155413-1-8 (2011).
(10) Korn, T., Heydrich, S., Hirmer, M., Schmutzler, J. & Schüller, C. Low-temperature photocarrier dynamics in monolayer MoS_2. *Appl. Phys. Lett.* **99**, 102109-1-3 (2011).
(11) Ghatak, S., Pal, A. N. & Ghosh, A. Nature of electronic states in atomically thin MoS_2 field-effect transistors. *ACS Nano* **5,** 7707-7712 (2011).
(12) Eda, G., Yamaguchi, H., Voiry, D., Fujita, T., Chen, M. & Chhowalla, M. Photoluminescence from chemically exfoliated MoS_2. *Nano Lett.* **11,** 5111−5116 (2011).
(13) Zeng, H., Dai, J., Yao, W., Xiao, D. & Cui, X. Valley polarization in MoS_2 monolayers by optical pumping. *Nat. Nanotechnol.* **7,** 490 (2012).
(14) Pu. J., Yomogida, Y., Liu, K.-K., Li, L.-J., Iwasa, Y. & Takenobu, T. Highly flexible MoS_2 thin-film transistors with ion gel dielectrics. *Nano Lett.* **12,** 4013–4017 (2012).
(15) Mak, K. F., He, K., Lee, C., Lee, G. H., Hone, J., Heinz, T.F. & Shan, J. Tightly bound trions in monolayer MoS_2. *Nature Mater.* **12,** 207–211 (2013).
(16) Zhang, W., Chuu, C.-P., Huang, J.-K., Chen, C.-H., Tsai, M.-L., Chang, Y.-H., Liang, C.-T., He, J.-H., Chou, M.-Y. & Li, L.-J. Ultrahigh-gain phototransistors based on graphene-MoS_2 heterostructures. *arXiv preprint arXiv:1302.1230* (2013).
(17) Radisavljevic, B., Radenovic, A., Brivio, J., Giacometti, V. & Kis, A. Single-layer MoS_2 transistors. *Nat. Nanotechnol.* **6,** 147-150 (2011).
(18) Radisavljevic, B., Whitwick, M. B. & Kis, A. Integrated circuits and logic operations based on single-layer MoS_2. *ACS Nano* **5,** 9934-9938 (2011).
(19) Fang, H., Chuang, S., Chang, T. C., Takei, K., Takahashi, T. & Javey, A. High-performance single layered WSe_2 p-FETs with chemically doped contacts. *Nano Lett.* **12,** 3788−3792 (2012).

(20) Podzorov, V., Gershenson, M. E., Kloc, Ch., Zeis, R. & Bucher, E. High-mobility field-effect transistors based on transition metal dichalcogenides. *Appl. Phys. Lett.* **84,** 3301 (2004).
(21) Liu, W., Kang, J., Sarkar, D., Khatami, Y., Jena, D. & Banerjee, K. Role of metal contacts in designing high-performance monolayer n-type WSe_2 field effect transistors. *Nano Lett.* doi: 10.1021/nl304777e (2013).
(22) Glemser, O., Sauer, H. & König, P. Über wolframsulfide und wolframselenide. *Z. Anorg. Chem.* **257,** 241–246 (1948).
(23) Schäfer, H., Wehmeier, F. & Trenkel, M. Chemischer transport mit schwefel als transportmittel. *J. Less-Common Met.* **16,** 290 (1968).
(24) Al-Hilli, A.A. & Evans, B.L. The preparation and properties of transition metal dichalcogenide single crystals. *J. Cryst. Growth* **15,** 93 (1972).
(25) Brixner, L.H. Preparation and properties of the single crystalline AB_2-type selenides and tellurides of niobium, tantalum, molybdenum and tungsten. *J. Inorg. Nucl. Chem.* **24,** 257 (1962).
(26) Brixner, L.H. X-ray study and thermoelectric properties of the $W_xTa_{1-x}Se_2$ system. *J. Electrochem. Soc.* **110,** 289-293 (1963).
(27) Hicks, W. T. Semiconducting behavior of substituted tungsten diselenide and its analogues. *J. Electrochem. Soc*. **111,** 1058 (1964).
(28) Merzhanov, A. G. Properties of WSe_2 produced by self-propagating high-temperature synthesis. *Izv. Akad. Nauk SSSR, Neorg. Mater.* **13,** 811-814 (1977).
(29) Obolonchik, V. A. & Prokoshink, L.M. Synthesis of selenides of the transition metals by the interaction of the oxides with hydrogen selenide. *Zh. Prikl. Khim. Leningrad* **44,** 2160 (1971).
(30) Tsirlina, T., Feldman, Y., Homyonfer, M., Sloan, J., Hutchison, J.L. & Tenne, R. Synthesis and characterization of inorganic fullerene-like WSe_2 material. *Fullerene Sci. Technol.* **6,** 157 (1998).
(31) Lee, Y. H., Zhang, X. Q., Zhang, W., Chang, M. T., Lin, C. T., Chang, K. D., Yu, Y.-C., Wang, T. W., Chang, C.-S., Li, L. J. & Lin, T. W. Synthesis of large-area MoS_2 atomic layers with chemical vapor deposition. *Adv. Mater.* **24,** 2320−2325 (2012).
(32) Lee, Y.-H., Yu, L., Wang, H., Fang, W., Ling, X., Shi, Y., Lin, C.-T., Huang, J.-K., Chang, M.-T., Chang, C.-S., Dresselhaus, M., Palacios, T., Li, L.-J. & Kong, J. Synthesis and transfer of single layer transition metal disulfides on diverse surfaces *Nano Lett.* **13,** 1852-1857 (2013).
(33) Lin, Y.-C., Zhang, W., Huang, J.-K., Liu, K.-K., Lee, Y.-H., Liang, C.-T., Chu, C.-W. & Li, L.-J. Wafer-scale MoS_2 thin layers prepared by MoO_3 sulfurization. *Nanoscale* **4,** 6637 (2012).
(34) Seo, J., Jun, Y., Park, S., Nah, H., Moon, T., Park, B., Kim, J.-G., Kim, Y. J. & Cheon, J. Two-dimensional nanosheet crystals. *Angew. Chem. Int. Ed.* **46,** 8828−8831 (2007).
(35) Li, H., Lu, G., Wang, Y., Yin, Z., Cong, C., He, Q., Wang, L., Ding, F., Yu, T. & Zhang, H. Mechanical exfoliation and characterization of single- and few-layer nanosheets of WSe_2, TaS_2, and $TaSe_2$. *Small* doi: 10.1002/smll.201202919 (2012).
(36) Mead, D. G. & Irwin, J. C. Long wavelength optic phonons in WSe_2. *Can. J. Phys.* **55,** 379-382 (1977).
(37) Sourisseau, C., Cruege, F., Fouassier, M. & Alba, M. Second-order Raman effects, inelastic neutron scattering and lattice dynamics in 2H-WS_2. *Chem. Phys.* **150,** 281 (1991).

(38) Frey, G. L., Tenne, R., Matthews, M. J., Dresselhaus, M. S. & Dresselhaus, G. Raman and resonance Raman investigation of MoS_2 nanoparticles. *Phys. Rev. B* **60,** 2883 (1999).
(39) Sekine, T., Izumi, M., Nakashizu, T., Uchinokura, K. & Matsuura, E. Raman scattering and infrared reflectance in 2H-$MoSe_2$. *J. Phys. Soc. Jpn.* **49,** 1069 (1980).
(40) Lee, C., Yan, H., Brus, L. E., Heinz, T. F., Hone, J. & Ryu, S. Anomalous lattice vibrations of single-and few-layer MoS_2. *ACS Nano* **4,** 2695-2700 (2010).
(41) Zhao, W., Ghorannevis, Z., Chu, L., Toh, M., Kloc, C., Tan, P.-H. & Eda, G. Evolution of electronic structure in atomically thin sheets of WS_2 and WSe_2. *ACS Nano* **7,** 791–797 (2013).
(42) Beal, A. R., Knights, J. C. & Liang, W. Y. Transmission spectra of some transition metal dichalcogenides. II. Group VIA: trigonal prismatic coordination. *J. Phys. C: Sol. Stat. Phys.* **5,** 3540 (1972).
(43) Bromley, R. A., Murray, R. B. & Yoffe, A. D. The band structures of some transition metal dichalcogenides. III. GroupVIA: trigonal prism materials. *J. Phys. C: Sol. Stat. Phys.* **5,** 759 (1972).
(44) Kuc, A., Zibouche, N. & Heine, T. Influence of quantum confinement on the electronic structure of the transition metal sulfide TS_2. *Phys. Rev. B* **83,** 245213 (2011).
(45) Jiang, H. Electronic band structures of molybdenum and tungsten dichalcogenides by the GW approach. *J. Phys. Chem. C* **116,** 7664–7671 (2012).
(46) Zeng, H., Liu, G.-B., Dai, J., Yan, Y., Zhu, B., He, R., Xie, L., Xu, S., Chen, X., Yao, W. & Cui, X. Optical signature of symmetry variations and spin-valley coupling in atomically thin tungsten dichalcogenides. *arXiv preprint arXiv:1208.5864.* (2012).
(47) Salitra G., Hodes G., Klein E. & Tenne R. Highly oriented WSe_2 thin films prepared by selenization of evaporated WO_3. *Thin Solid Films* **245,** 180 (1994).
(48) Schellenberger, A., Schlaf, R., Mayer, T., Holub-Krappe, E., Pettenkofer, C., Jaegermann, W., Ditzinger, U.A. & Neddermeyer, H. Na adsorption on the layered semiconductors SnS_2 and WSe_2. *Surf. Sci.* **241,** L25 (1991).
(49) Hulliger, F. *Structural chemistry of the layer-type phases*; Levy, F., Ed.; Reidel, 1976.
(50) Xia, J., Chen, F., Li, J. & Tao, N. Measurement of the quantum capacitance of graphene *Nat. Nanotechnol.* **4,** 505–509 (2009).
(51) Traving, M., Boehme, M., Kipp, L., Skibowski, M., Starrost, F., Krasovskii, E. E., Perlov, A. & Schattke, W. Electronic structure of WSe_2: A combined photoemission and inverse photoemission study. *Phys. Rev. B* **55,** 10392 (1997).
(52) Radisavljevic, B., Whitwick, M. B. & Kis, A. Integrated circuits and logic operations based on single-layer MoS_2. *Nano Lett.* **5**, 9934 (2011).
(53) Kohn W. & Sham, L. J. Self-Consistent Equations Including Exchange and Correlation Effects. *Phys. Rev.* **140,** A1133 (1965).
(54) Kresse, G. & Furthmüller, J. Efficiency of ab-initio total energy calculations for metals and semiconductors using a plane-wave basis set. *Comput. Mater. Sci.* **6,** 15-50 (1996).
(55) Kresse, G. & Furthmüller, J. Efficient iterative schemes for ab initio total-energy calculations using a plane-wave basis set. *Phys. Rev. B* **54,** 11169 (1996).
(56) Blöchl, P. E. Projector augmented-wave method. *Phys. Rev. B* **50,** 17953 (1994).
(57) Ceperley, D. M. & Alder, B. J. Ground State of the Electron Gas by a Stochastic Method. *Phys. Rev. Lett.* **45,** 566 (1980).

Supporting Materials

Large-Area and Highly Crystalline WSe_2 Monolayers: from Synthesis to Device Applications

By Jing-Kai Huang,[12] Jiang Pu,[3] Chih-Piao Chuu,[1] Chang-Lung Hsu, [1] Ming-Hui Chiu[1], Zhen-Yu Juang,[1] Yong-Huang Chang,[1] Wen-Hao Chang,[4] Yoshihiro Iwasa,[5] Mei-Ying Chou,[1,6,7] Taishi Takenobu[3] and Lain-Jong Li[1]**

[1]*Institute of Atomic and Molecular Sciences, Academia Sinica, Taipei, 10617, Taiwan*

[2] *Department of Photonics, National Chiao-Tung University, HsinChu, 300, Taiwan*

[3] *Department of Applied Physics, Waseda University, Tokyo 169-8555, Japan*

[4] *Department of Electrophysics, National Chiao-Tung University, HsinChu, 300, Taiwan*

[5]*Department of Applied Physics, The University of Tokyo, Tokyo 113-8656, Japan*

[6]*Department of Physics, National Taiwan University, Taipei, Taiwan*

[7]*School of Physics, Georgia Institute of Technology, Atlanta, GA 30332, USA*

To whom correspondence should be addressed: (T.Takenobu) takenobu@waseda.jp; (L. J. Li) lanceli@gate.sinica.edu.tw

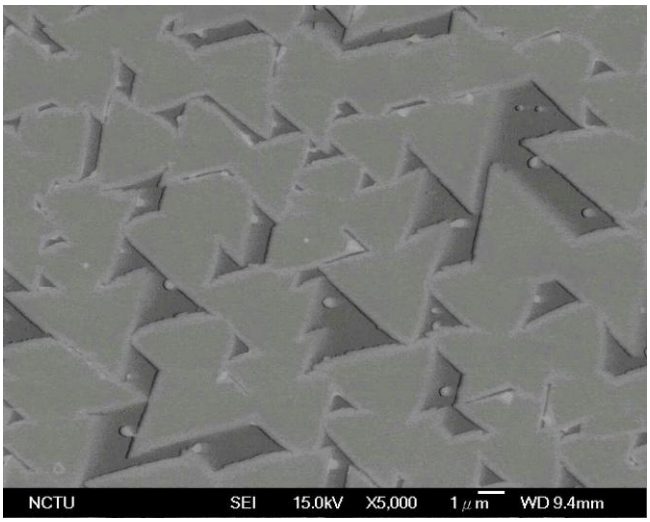

Figure S1. The SEM image for the morphology of the WSe_2 grown at 750^{o}C before it is completely merged.

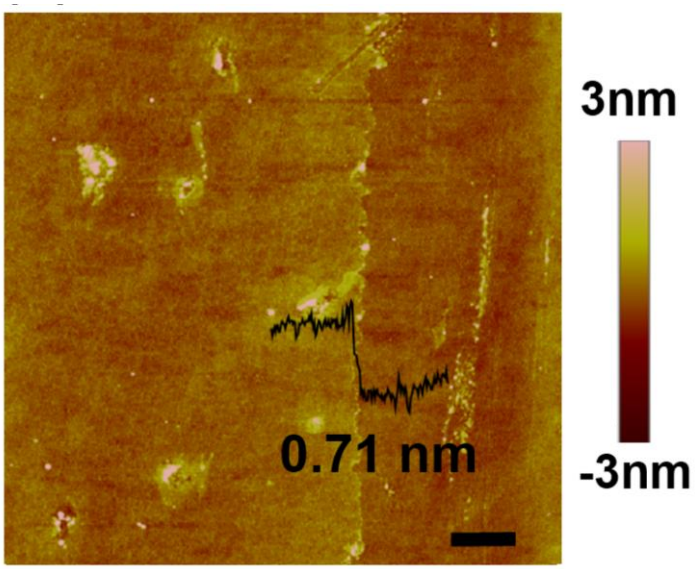

Figure S2. The AFM image for the WSe_2 monolayer film grown at 750^{o}C, where we made a scratch on the right hand side in the image. The step height between WSe_2 and the substrate is 0.71 nm.

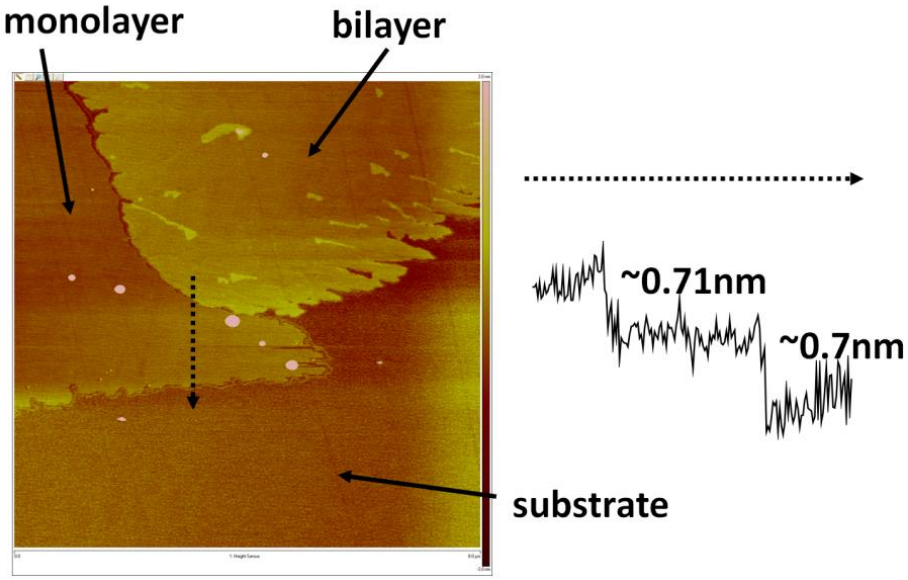

Figure S3. The AFM cross-sectional height profile for the WSe_2 bilayer sample shown in Figure 2a,where the thickness of the top layer grown on the bottom layer is ~ 0.71 nm.

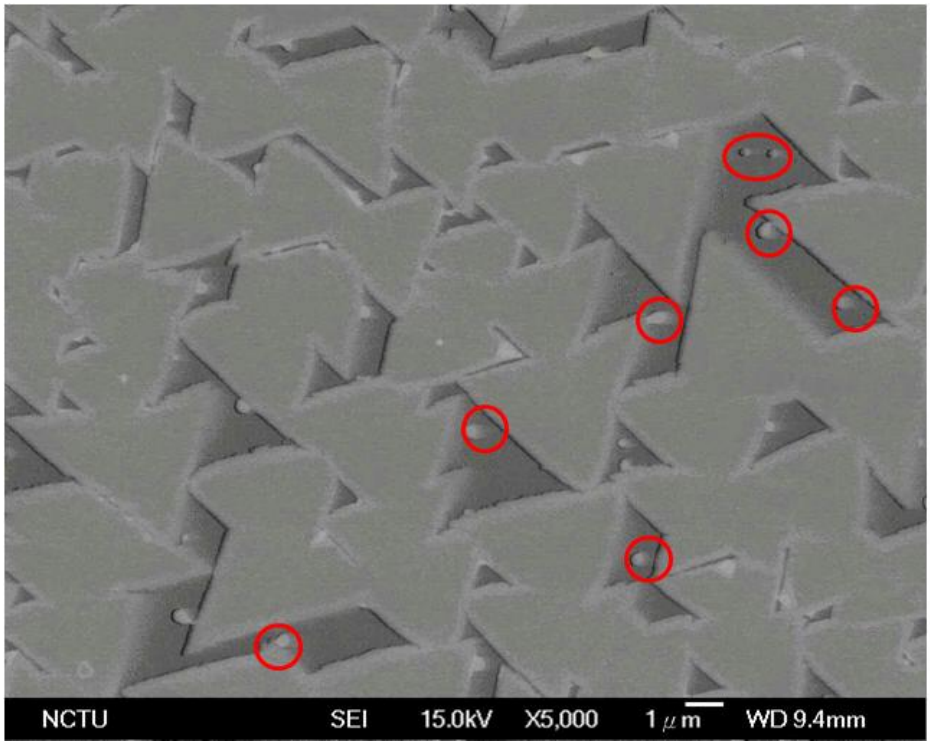

Figure S4. The SEM image showing the formation of some WO_3 particles, as indicated by the circles in graph, during the growth of WSe_2 film.

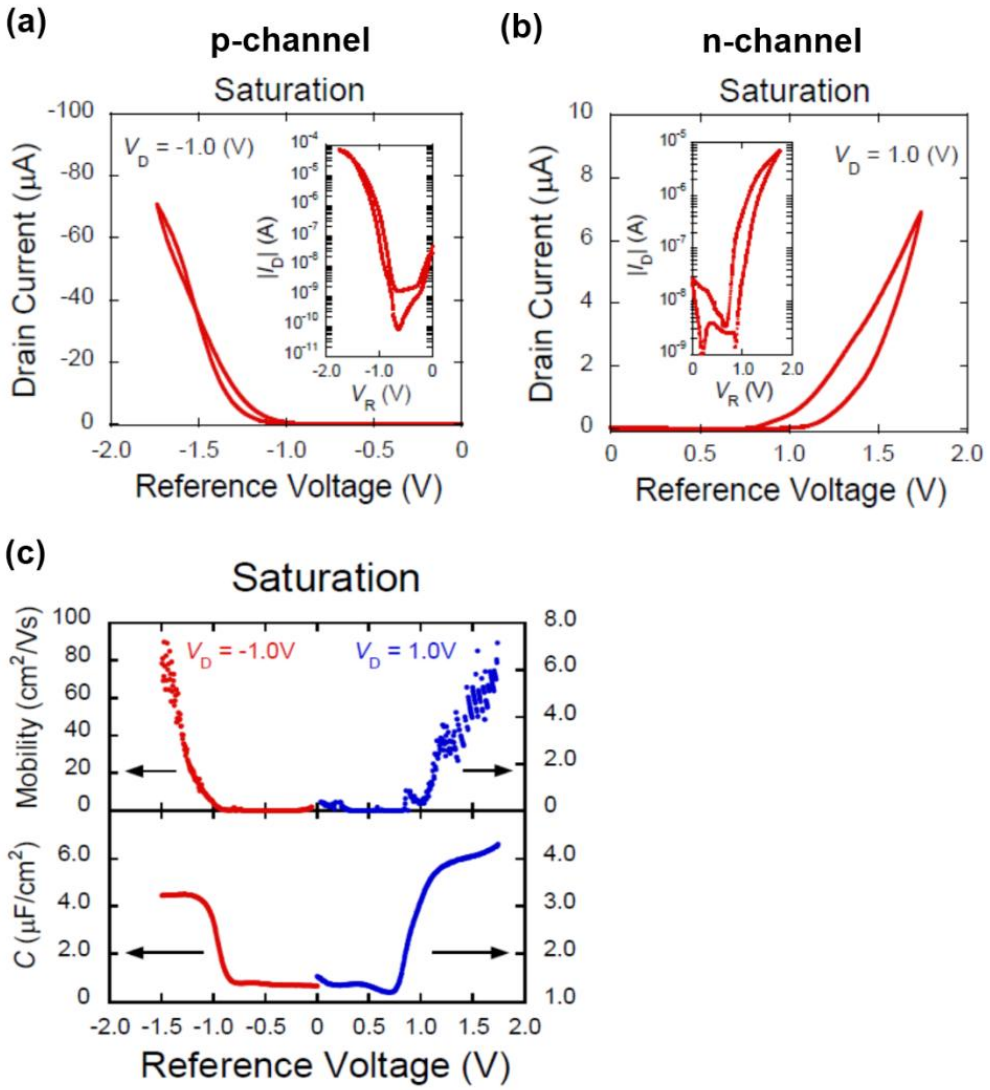

Figure S5. (a,b) The transfer curves, (c) mobility and capacitance dependences on V_R performed in the saturation regime for the same device discussed in text (Figure 4).